GAMM-Mitt. **30**, No. 1, 171 – 184 (2007)

Linear and nonlinear approach to the Rosensweig instability

Adrian Lange[*1], **Reinhard Richter**[**2], and **Lutz Tobiska**[***3]

[1] Fraunhofer Institute for Material and Beam Technology, Winterbergstraße 28, D-01277 Dresden, Germany

[2] Experimentalphysik V, Universität Bayreuth, D-95440 Bayreuth, Germany

[3] Institute of Analysis and Numerical Mathematics, Otto-von-Guericke University Magdeburg, D-39016 Magdeburg, Germany

Key words magnetic fluids, ferrofluid, interfacial instability, Rosensweig instability, pattern formation, hydrodynamic stability, solitons, finite elements.

We report on recent efforts to improve the understanding of the Rosensweig instability in the linear as well as in the nonlinear regime. In the linear regime we focus on the wavenumber of maximal growth and the oscillatory decay of metastable magnetic liquid ridges, accessible via a new pulse technique. We compare the measurements with the predictions of the linear stability analysis. In the nonlinear regime the fully developed Rosensweig pattern was successfully estimated by the method of finite elements, taking into account the nonlinear magnetization law. For a comparison with these results the three-dimensional surface profile is recorded by a radioscopic measurement technique. The bifurcation diagram measured in this way can be fitted by the roots of an amplitude equation. Eventually we investigate ferrosolitons, which were recently uncovered in the bistability interval of the Rosensweig instability.

1 Introduction

The formation of static liquid mountains, floating on the free surface of a magnetic fluid (MF), when subjected to a vertical magnetic field is a fascinating phenomenon, as shown in Fig. 1. This is mainly because it is at the first glance counterintuitively: the new surface profile has an increased surface- and hydrostatic energy. However, this can be understood, by taking into account *all* contributing energies. A horizontal layer of MF in a vertically applied magnetic induction B is characterized by the energy density [1, 2]:

$$\begin{aligned}\mathcal{F}[h(x,y)] &= \frac{\rho g}{2}h^2(x,y) - \int_0^h dz B\frac{\mu_\mathrm{r}-1}{2}H_\mathrm{MF}(x,y,z) \\ &\quad +\sigma\sqrt{1+(\partial_x h(x,y))^2+(\partial_y h(x,y))^2}. \end{aligned} \tag{1}$$

* e-mail: adrian.lange@iws.fraunhofer.de, Phone: +49 351 258 3328

** e-mail: reinhard.richter@uni-bayreuth.de, Phone +49 921 553351

*** e-mail: Lutz.Tobiska@mathematik.uni-magdeburg.de, Phone +49 391 67-18650

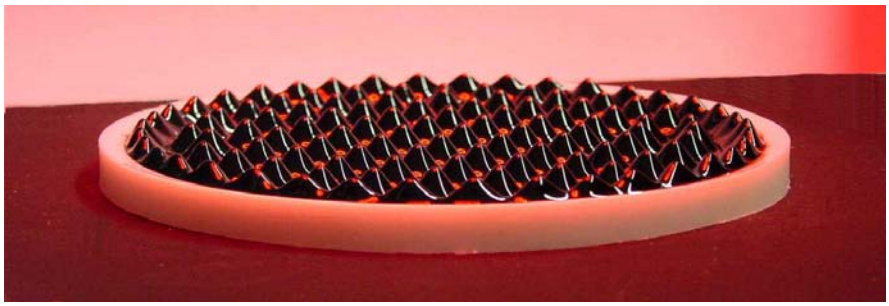

Fig. 1 Peaks of magnetic fluid at a supercritical induction $B > B_c$ in a Teflon® vessel with a diameter of 12 cm. Picture taken at Universität Bayreuth by B. Reimann.

Here ρ and σ are the density and surface tension of the MF, $h(x, y)$ the local height of the liquid layer, and $H_{\mathrm{MF}}(x, y, z)$ is the magnetic field in the presence of the MF. The three terms in Eq. (1) represent the hydrostatic, magnetic and surface energy, respectively. As the surface profile deviates from the flat reference state, the first and last term grow whereas the magnetic energy decreases. For sufficiently large $B > B_c$, this gives rise to the normal field, or Rosensweig, instability [3, 4]. By minimizing the energy funcional of Eq. (1) the following amplitude equation can be derived [2]

$$\epsilon A + \gamma(1+\epsilon)A^2 - gA^3 = 0, \tag{2}$$

where $\epsilon = (B^2 - B_c^2)/B_c^2$ is the bifurcation parameter, and γ, g are scaling parameters.

The solutions of Eq. (2) are scetched in Fig.2(a). The stable branch characterizes a subcritical bifurcation to hexagons. In addition there are two unstable solutions which are connected to ridges and squares. Due to the *subcriticality* of the stable branch a quantitative description of the Rosensweig instability is a non-trivial task, both in experiment and theory:

A *linear description* of the Rosensweig instability is amenable in theory, but restricted to small amplitudes. In experiments they can be observed only for a very short time, during the increase of the pattern, because of the supercritical bifurcation. Thus a new pulse technique, scetched in Fig.2(b), has been developed and applied. Section 2 is devoted to the theory and experiments of the wavenumber of maximal growth and to the decay of metastable patterns within the linear regime.

A *nonlinear description* of the instability is necessary, in order to estimate the shape of the spikes and to determine what particular final pattern (hexagons, squares) occurs due to the complex *nonlinear* interactions. Despite some recent progress [2, 6] the theoretical description is still restricted to small relative permeabilities ($\mu_r < 1.4$) and a linear magnetization law. Thus a full numerical approach to the nonlinear problem, based on the finite element method is most welcome, as presented in section 3.1. For a comparison with experiments it is important that this method is capable to take into account the nonlinear magnetization law. From an experimental point of view, the nonlinear properties are difficult to access because the dark and steep patterns are an obstacle for standard optical measurement techniques. Thus we utilize the absorption of x-rays, in order to record the full surface profile and the bifurcation diagram. In addition we present in 3.2 newly detected solitary surface patterns within the bistable regime of the Rosensweig instability.

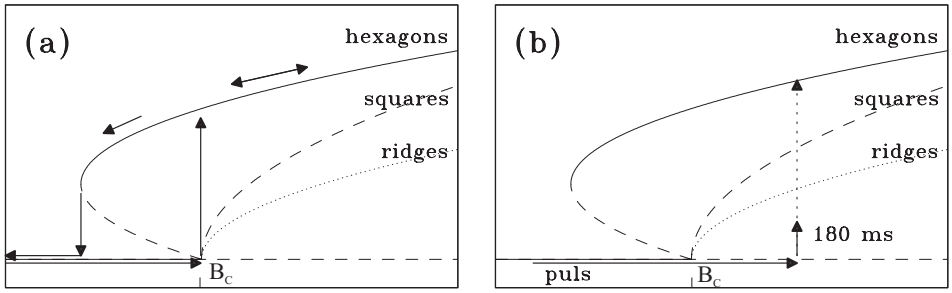

Fig. 2 Scheme of the bifurcation diagram in the vicinity of the bifurcation point B_c, as predicted by [1] and [2]. Figure (**a**) illustrates an adiabatic change of the control parameter B, (**b**) the consequences of a jump-like increase. From Ref. [5].

2 Linear pattern formation

Most experimentalists were following the pioneers [3] by varying the magnetic induction in a quasi static manner. By moving on the hysteretic path, sketched in Fig. 2(a), they were focusing on the nature of the stable pattern in the nonlinear regime [7, 8]. The wavenumber observed in this way was found to be independent from the strength of the supercritical induction [3, 7, 9]. Unfortunately this result had been compared with the predictions of the linear theory [10]. However, the final stable pattern, resulting from *nonlinear* interactions, does not generally correspond to the most unstable *linear* pattern. For a successful comparison with the predictions of the linear theory [11, 12], not fully developed rigdes of small amplitude are suitable. In accordance with the bifurcation diagram, they are the first metastable pattern which emerge after a jump-like increase of the induction, as sketched in Fig. 2(b). In this way different aspects of the linear part of the pattern forming process are studied experimentally as well as theoretically, allowing a *quantitative* comparison of the corresponding results (Sect. 2.2 and 2.3).

2.1 System and basic equations

A horizontally unbounded layer of an incompressible, nonconducting, and viscous magnetic fluid of thickness h and constant density ρ is considered. The fluid is bounded from below by the bottom of a container made of a magnetically impermeable material and has a free surface with air above. The electrically insulating fluid justifies the stationary form of the Maxwell equations, which reduce to the Laplace equation for the magnetic potentials in the region of the container, the magnetic fluid, and the air. It is assumed that the magnetization $\mathbf{M}$ of the magnetic fluid depends linearly on the applied magnetic field $\mathbf{H}$, $\mathbf{M} = (\mu_r - 1)\mathbf{H}$, where μ_r is the relative permeability of the fluid.

In a linear stability analysis, all small disturbances from the basic state are decomposed into normal modes, i.e., into components of the form $\exp[-i(\omega\, t - \mathbf{q}\, \mathbf{r})]$, where $\mathbf{r} = (x, y)$ and the wave number is the absolute value of the wave vector, $q = |\mathbf{q}|$. With $\omega = \omega_1 + i\omega_2$, the real part of $-i\omega$, ω_2, is called the growth rate und defines whether the disturbances will grow ($\omega_2 > 0$) or decay ($\omega_2 < 0$). The absolute value of the imaginary part of $-i\omega$, $|\omega_1|$,

gives the angular frequency of the oscillations if it is different form zero. The linear stability analysis leads to the dispersion relation [13, 14, 15]

$$\begin{aligned} 0 \;=\; & \frac{\nu^2}{\tilde{q}\coth(\tilde{q}h) - q\coth(qh)} \Big\{ \tilde{q}\left[4q^4 + (q^2+\tilde{q}^2)^2\right]\coth(\tilde{q}h) - q\big[4q^2\tilde{q}^2 + \\ & + (q^2+\tilde{q}^2)^2\big]\tanh(qh) - \frac{4q^2\tilde{q}(q^2+\tilde{q}^2)}{\cosh(qh)\sinh(\tilde{q}h)} \Big\} \\ & + \tanh(qh)\left[gq + \frac{\sigma}{\rho}q^3 - \frac{\mu_0\mu_r M^2}{\rho}\Lambda(qh)\,q^2\right], \end{aligned} \tag{3}$$

where ν is the kinematic viscosity, M the absolute value of the magnetisation, $\mathbf{g} = (0, 0, -g)$ the acceleration due to gravity, μ_0 the permeability of free space, $\tilde{q} = \sqrt{q^2 - i\omega/\nu}$, and $\Lambda(qh) = [\mathrm{e}^{qh}(1+\mu_r) + \mathrm{e}^{-qh}(1-\mu_r)]/[\mathrm{e}^{qh}(1+\mu_r)^2 - \mathrm{e}^{-qh}(1-\mu_r)^2]$. The condition of marginal stability, $\omega = 0$, defines the critical quantities at which the Rosensweig instability occurs. In the limit of an infinitely thick ($h \to \infty$) layer the critical induction and the wave number, respectively, are

$$B_{c,\infty}^2 = \frac{2\mu_0\,\mu_r(\mu_r+1)\sqrt{\rho\,\sigma\,g}}{(\mu_r-1)^2} \qquad\qquad q_c = \sqrt{\frac{\rho\,g}{\sigma}}\,. \tag{4}$$

These critical values for the *onset* of the instability apply for viscous as well as for inviscid magnetic fluids.

2.2 Growing ridges

Generally it is assumed that in the linear stage of the pattern forming process the wave number with the largest growth rate will prevail. Therefore this mode is called linearly most unstable mode. Due to its role in the pattern formation it is of particular interest to examine the wave number of maximal growth, q_m, and its dependence on the different parameters as supercritical induction and viscosity.

For a general analysis it is advantageous to consider the dimensionless form (indicated by the bar) of the dispersion relation (3) in the limit $h \to \infty$ for growing disturbances, i.e. $\omega = i\omega_2$ with $\omega_2 > 0$,

$$\left(\bar{\nu} + \frac{\bar{\omega}_2}{2\bar{q}^{\,2}}\right)^2 + \frac{\bar{q} + \bar{q}^{\,3} - 2\bar{B}^2\bar{q}^{\,2}}{4\bar{q}^{\,4}} - \bar{\nu}^2\sqrt{1 + \frac{\bar{\omega}_2}{\bar{\nu}\bar{q}^{\,2}}} = 0\,. \tag{5}$$

All lengths were scaled with $[\sigma/(\rho\,g)]^{1/2}$, the time with $\sigma^{1/4}/(g^{3/4}\rho^{1/4})$, the viscosity with $\sigma^{3/4}/(g^{1/4}\rho^{3/4})$, and the induction with $B_{c,\infty}$. The solution of Eq. (5) for three different supercritical inductions is shown in Fig. 3(a). One can clearly see that the maximum of the curves, given by $\bar{q}_m$ and $\bar{\omega}_{2,m}$, is increasing monotonously with the induction $\bar{B}$. The wave number of maximal growth, defined by $\partial\bar{\omega}_2/\partial\bar{q} = 0$, is a monotonously increasing quantity for increasing fields and all viscosities with the exception of the limit $\bar{\nu} \to \infty$ [Fig. 3(b)]. The change of $\bar{q}_m$ for a fixed difference of the supercritical induction is largest for inviscid MFs [see upper dot-dashed line in Fig. 3(b)] and shrinks with increasing viscosity. For low viscous MFs, $\bar{q}_m$ depends linearly on $\bar{B}$ as long as $\bar{B}$ is not too large. The main result of Fig. 3(b) is that for a *quantitative* analysis of real MFs, represented here by $\bar{\nu} = 0.037$, the description

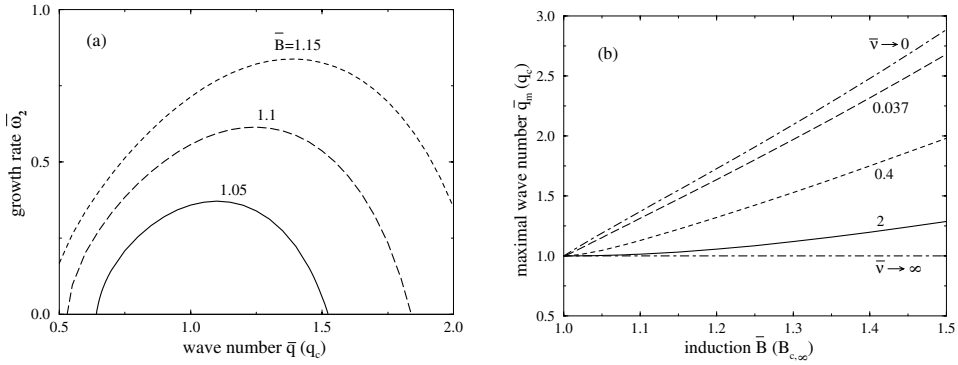

Fig. 3 (a) Positive growth rate $-i\bar{\omega} = \bar{\omega}_2$ as function of the wave number $\bar{q}$ for $\bar{\nu} = 0.037$, typically for MFs in experiments [16]. (b) Maximal wave number $\bar{q}_m$ as a function of the supercritical induction $\bar{B}$ for different viscosities. $\bar{q}_m$ is a monotonously increasing function of $\bar{B}$ with the exception $\bar{q}_m = 1$ [10] in the case of infinitely large viscosities (lower dot-dashed line). In the limit of an inviscid fluid (upper dot-dashed line) the dependence of $\bar{q}_m$ on $\bar{B}$ is given by $\bar{q}_m = (1/3)\left(2\bar{B}^2 + \sqrt{4\bar{B}^4 - 3}\right)$ [14].

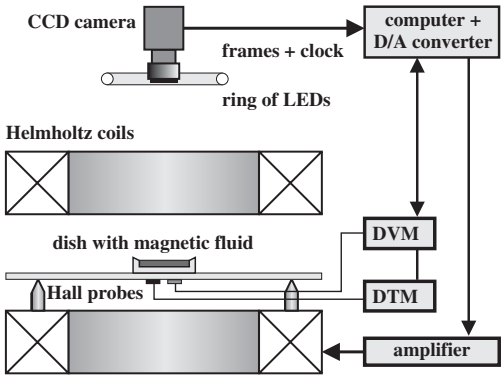

Fig. 4 Scheme of the experimental setup.

by the limit cases is insufficient. For a *qualitative* analysis, the limit $\bar{\nu} \to 0$ gives the correct trend.

In order to test these predictions, we are measureing the wavenumber of maximal growth with the setup shown in Fig. 4. A cylindrical Teflon® vessel with the radius 60 mm and depth of 2 mm is filled with MF up to the brim and positioned in the center of a pair of Helmholtz coils. The MF is illuminated from above by a ring of LEDs placed above the surface. A CCD camera is mounted in the center of the ring. In this way only an inclined surface of proper angle will reflect light into the camera lens, but a flat fluid surface reflects no light in this direction. In the theory the supercritical magnetic field is assumed to be instantly increased. In the experiment a jump-like increase could be realized within 80 ms, by utilizing a thyristor

controlled amplifier (fug Elektronik GmbH). This is much shorter than the viscous time scale of 450 ms. For details see Ref. [11].

Fig. 5 Three snapshots of the principal pattern evolution on the MF for a jump-like increase towards a supercritical induction. The pictures are taken $\Delta t = 180$ ms (a), 280 ms (b), 560 ms (c) after the start of the increase of the magnetic field. Pictures from Ref. [11].

Figure 5(a) shows circular surface deformations taken $\Delta t = 180\,\mathrm{ms}$ after the start of the experiment. These surface deformations are first created at the edge of the dish, because of the discontinuity of the magnetic induction induced by the finite size of the container. With increasing time more circular deformations evolve, approaching the centre of the dish [see Fig. 5(a)]. Onto this pattern, Rosensweig peaks emerge out of the crests of the circular surface deformation, as can be seen in Fig. 5(b). After this transient concentric arrangement, a hexagonal pattern of Rosensweig peaks evolves [see Fig. 5(c)].

The wave number of the concentric deformed region in Fig. 5(a) is determined from the experiment (for details see [11]) and compared with the theoretical calculation of the wave number with maximal growth. For the calculations we used a layer thickness of $h = 2$ mm and the material parameters of the magnetic fluid EMG 909, namely $\rho = 1.02 \cdot 10^3\ \mathrm{kg\,m^{-3}}$, $\nu = 5.88 \cdot 10^{-6}\ \mathrm{m^2\,s^{-1}}$, $\sigma = 2.65 \cdot 10^{-2}\ \mathrm{kg\,s^{-2}}$, $\mu_r = 1.8$, (dashed line in Fig. 6). The comparison with the experimental data (open squares) shows that the correct linear slope starting at the critical wave number q_c is reproduced, but the critical induction is too large. Since q_c depends on the fluid density and the surface tension [see Eq. (4)] and the viscosity does not influence the critical quantities, the relative permeability μ_r is the only remaining fit parameter. Using $\mu_r \simeq 1.85$ (solid line), a rather good agreement between the experimental results and the theoretical graph is achieved. The fitted value for μ_r differs by 2.8% from the value given by the producer, a deviation which is well within the tolerance specified by producer. In this way, the most unstable linear pattern could be detected in the experiment and the theoretically predicted linear dependence of q_m on the magnetic induction was confirmed.

2.3 Decaying ridges

In this section we are studying the fate of the linear most unstable pattern when switching to a subcritical induction. Particularly, the oscillatory decay of magnetic liquid ridges [11] towards a flat surface is observed. It turns out that the oscillation frequency and the propagation velocity of the decaying pattern depends sensitively on the subcritical magnetic induction. When approaching the bifurcation point B_c from below, a dramatic decrease of both observable can be measured.

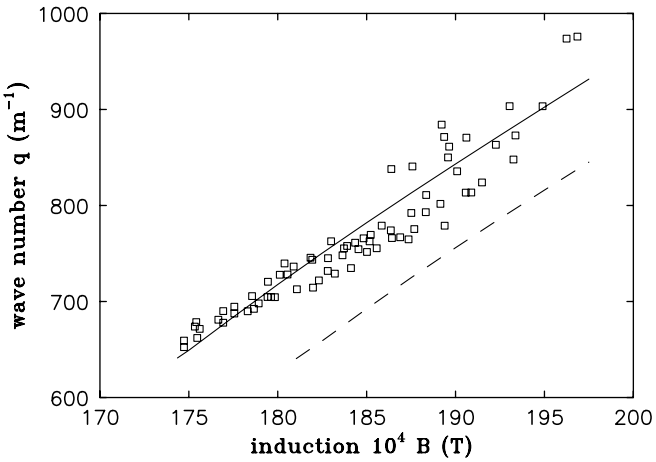

Fig. 6 Plot of the wave number q versus the magnetic induction B. The open squares give the experimental values, the dashed line displays the theoretical results for the material parameters of EMG 909 (see text). Using μ_r as a fit parameter gives the solid line. From Ref. [11].

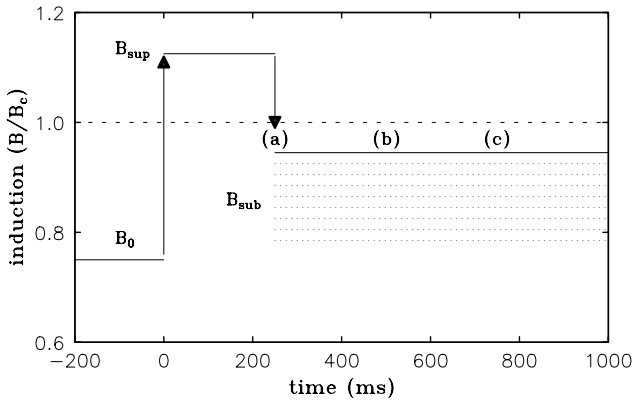

Fig. 7 Pulse sequence of the preparation of the liquid ridges. The small letters a, b, and c mark the times when the pictures of Fig. 8 were taken. From Ref. [12].

In order to prepare a state of unstable liquid ridges, the magnetic induction has to be switched in a jump-like manner to a supercritical value $B_{\rm sup}$, as sketched in Fig. 7. Before they start to develop into the hexagonal arrangement of peaks, the induction is switched back to a subcritical value $B_{\rm sub}$ (see Fig. 7). Now the liquid ridges decay in an oscillatory manner. Figure 8 shows half of such an oscillation period. The oscillation starts with a pattern of concentric liquid ridges, as presented in Fig. 8(a). Figure 8(b) shows the approximately flat surface after a quarter of the period. The liquid ridges after half of the period are displayed in Fig. 8(c).

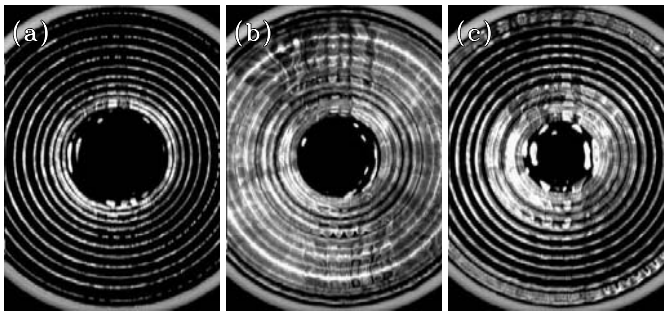

Fig. 8 Initial pattern of liquid ridges (a), approximately flat surface after a quarter of the oscillation period (b), and liquid ridges after half of the oscillation period (c).

From these pictures the oscillation frequency and the propagation velocity were extracted (for details see [12]). The square of the oscillation period as a function of the magnetic induction is shown in Fig. 9(a). Starting with a jump to the supercritical induction $B_{\rm sup} = 18$ mT, the oscillation period was measured for 12 different values of the subcritical induction. The measured data are denoted in Fig. 9(a) by open circles. The error bars are estimated from seven independent measurements. The data proof a square root like dependence from the induction, and are well described by the theory (solid line). A second measurement series has been performed for $B_{\rm sup} = 17.5$ mT. In this way a pattern of liquid ridges with a smaller wave number has been prepared. The data for these oscillation frequencies are marked in Fig. 9(a) by open squares. Again a good agreement between experimental data and theory is found. In a certain range of the vessel we observe propagating waves. The propagation

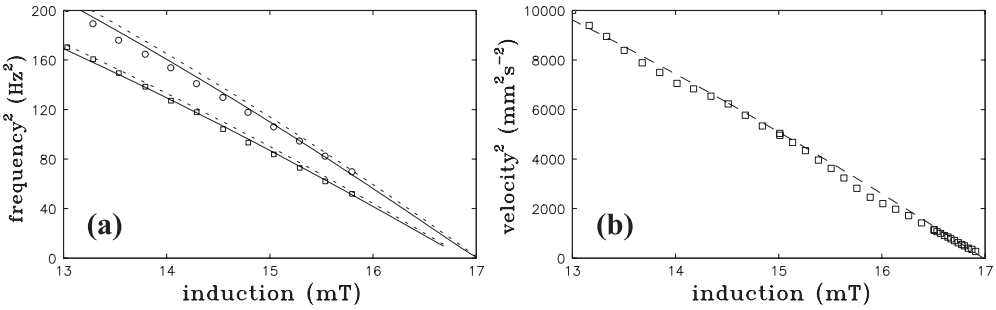

Fig. 9 (a) Square of the oscillation frequency of the liquid ridges versus the subcritical magnetic induction. The open circles (squares) denote the measured data obtained after a pulse of $B_{\rm sup} = 18$ mT (17.5 mT), respectively. A layer thickness of 3 mm was used. The solid (dashed) lines give the theoretical results for a viscous (inviscid) MF, respectively. (b) Square of the propagation velocity versus the subcritical magnetic induction. A preparing pulse of $B_{\rm sup} = 18$ mT and a layer thickness of 2 mm were used. The dashes line gives the best two-parameter fit for $\mu_r = 1.98$ and $h = 1.15$. From Ref. [12].

velocity has been extracted from the recorded pictures, as reported in Ref. [12]. In Fig. 9(b), the square of the propagation velocity is denoted by open squares and has been plotted versus

the subcritical induction. The data proof a square-root like scaling behaviour for a full decade of the velocity. In comparison with Fig. 9(a), this dependency could be corroborated even in the immediate vicinity of the bifurcation point. The dashed line gives the best two-parameter fit, yielding $\mu_r = 1.98$ and $h = 1.15$.

According to the experimental procedure, the solution of the dispersion relation (3) for a *super*critical induction has to be determined in order to calculate q_m, the wave number with maximal growth. Afterwards one has to solve the dispersion relation for a *sub*critical induction at that q_m which gives the relevant solution $\omega(q_m) = \omega_1(q_m) + i\omega_2(q_m)$ for the comparison with the experiment. Knowing $\omega_1(q_m)$, the frequency of the oscillation is given by $f = |\omega_1|/(2\pi)$ and the experimentally measured propagation velocity by $v = |\omega_1|/q_m$, respectively. The results of these calculations produce the theoretical graphs plotted in Fig. 9.

3 Nonlinear pattern formation

This paragraph is devoted to new numerical and experimental approaches to the fully developed patterns. We start with the numerics.

3.1 Numerical approach

First we scetch the basic equations, next we focus on the boundary conditions together with modeling aspects, eventually we discuss results for static and dynamic surface profiles.

3.1.1 System and basic equations

The Maxwell equations for a nonconducting fluid are given by

$$\text{curl}\,\mathbf{H} = \mathbf{0}, \quad \text{div}\,\mathbf{B} = 0 \qquad \text{in}\ \mathbb{R}^3, \tag{6}$$

with the magnetic field strength $\mathbf{H}$ and the magnetic induction $\mathbf{B}$ satisfying the constitutive relation

$$\mathbf{B} = \begin{cases} \mu_0(\mathbf{M}+\mathbf{H}) & \text{in} \quad \Omega_f(t), \\ \mu_0\mathbf{H} & \text{outside} \quad \Omega_f(t), \end{cases}$$

where $\Omega_f(t)$ is the time-dependent subdomain of $\mathbb{R}^3$ filled with the magnetic fluid at time t. The magnetization $\mathbf{M}$ is assumed to be parallel to the magnetic field and to follow the Langevin law,

$$M = |\mathbf{M}| = M_s \left(\coth(\gamma|\mathbf{H}|) - \frac{1}{\gamma|\mathbf{H}|} \right) \frac{\mathbf{H}}{|\mathbf{H}|},$$

with the saturation magnetization M_s, the Langevin parameter $\gamma = 3\chi_0/M_s$, and the initial susceptibility χ_0. As usual, instead of solving (6) numerically, we look for a magnetostatic potenial φ with $\mathbf{H} = -\nabla\varphi$ satisfying a nonlinear elliptic equation of the form

$$-\text{div}\ (\mu(x, |\nabla\varphi|)\nabla\varphi) = 0. \tag{7}$$

Note that the different magnetic properties of the magnetic fluid and the surrounding air causes a discontinuity of $\mu(\cdot, |\nabla\varphi|)$ across the interface between fluid and air which has to be taken

into account in designing an accurate numerical method. The hydrodynamic behaviour is described by the incompressible Navier-Stokes equations,

$$\rho\left(\mathbf{u}+(\mathbf{u}\cdot\boldsymbol{\nabla})\mathbf{u}\right) = \operatorname{div}\mathbf{T}(\mathbf{u},p,\mathbf{H})+\mathbf{f} \quad \text{in } \Omega_f(t)\ , \tag{8}$$

$$\operatorname{div}\mathbf{u} = 0 \quad \text{in } \Omega_f(t)\ , \tag{9}$$

where $\mathbf{T}(\mathbf{u},p,\mathbf{H})$ is the stress tensor with

$$\mathbf{T}(\mathbf{u},p,\mathbf{H}) = \eta\left(\nabla\mathbf{u}+\nabla\mathbf{u}^T\right)-\left(p+\frac{\mu_0}{2}|\mathbf{H}|^2\right)+\mathbf{B}\mathbf{H}\ .$$

Here, η denotes the dynamic viscosity, $\mathbf{u}$ the velocity, and p the pressure. The coupled system of partial differential equations has to be completed by appropriate boundary conditions, in particular the force balance and the kinematic condition at the free surface $\Gamma_f(t)$, i.e.,

$$[\mathbf{T}\cdot\mathbf{n}] = \sigma K\mathbf{n}, \quad \mathbf{u}\cdot\mathbf{n} = V_\Gamma, \qquad \text{on } \Gamma_f(t)$$

with the surface tension σ, the unit outer normal vector $\mathbf{n}$, the curvature of the free surface $K=\operatorname{div}\mathbf{n}$, and the normal velocity V_Γ of the free surface Γ_f. Often the air flow around the MF is neglected such that the force balance on the free surface simplifies to

$$\sigma K = [\mathbf{n}\cdot\mathbf{T}\cdot\mathbf{n}] \approx -2\eta\mathbf{n}\cdot\mathcal{D}(\mathbf{u})\mathbf{n}+p-p_0+\frac{\mu_0}{2}(\mathbf{M}\cdot\mathbf{n})^2\ , \tag{10}$$

$$(\mathcal{I}-\mathbf{n}\otimes\mathbf{n})\cdot\mathcal{D}(\mathbf{u})\mathbf{n} = 0\ , \tag{11}$$

where $\mathcal{D}(\mathbf{u})$ denotes the velocity deformation tensor given by

$$\mathcal{D}(\mathbf{u})_{ij} = \frac{1}{2}\left(\frac{\partial u_i}{\partial x_j}+\frac{\partial u_j}{\partial x_i}\right) \qquad i,j=1,\ldots,3,$$

$\mathcal{I}-\mathbf{n}\otimes\mathbf{n}$ the perpendicular projection into the tangential plane to the interface, p_0 the outer atmospheric pressure, and $\mathcal{I}$ the unit tensor.

3.1.2 Boundary conditions and modeling aspects

In the numerical study of surface instabilities it would be desirable to restrict the computational domain to the region of the magnetic fluid. However, we do not know the boundary conditions for the magnetostatic potential at the interface. Thus, we have to determine the potential inside and outside of the MF region by a discretization method, e.g. a finite element method. For this we need a finite computational domain. In case of the Rosensweig instability we can consider two different situations of an incompressible, nonconducting, and viscous fluid:

- a horizontally unbounded layer of infinite or finite thickness or
- a finite volume in a container.

The first case is closer to the theoretical setup of linear and nonlinear stability analysis whereas the second one mimics better the experimental setup. Let us discuss the first case. Taking into consideration that the applied field is perturbed by the pattern only locally in

a neighbourhood of the interface we can use in a sufficiently large distance $z = z_{\pm\infty}$ the boundary conditions for the undistorted case. For bounding the computational domain in the $x - y$ plane we consider only one cell of an developed pattern and use the corresponding wavelength as a characteristic length scale for the dimensionless computation. This approach has been successfully applied in [17, 18]. However, in this way it is impossible to find the preferred pattern, like hexagons, squares, or the newly observed solitons (see section 3.2 and Ref. [19]), respectively. The dynamics of growing ridges, as studied in section 2.2, can also not be handled in such a framework.

In the case of a finite volume in a container a combined finite element/ boundary element (BEM/FEM) approach can be applied for the calculation of the magnetostatic potential. The far field boundary conditions of the external field can be directly used in the BEM and nonlinear magnetization laws are taken into consideration by the FEM. For the study of shape deformation of a single axisymmetric droplet this technique has been used in [20]. However, the structure of developed pattern in the Rosensweig instability needs a much higher resolution of the computational domain and the use of adaptivity concepts seems to be compulsory.

3.1.3 Static and dynamic case

In the static case the magnetic fluid is in rest, $\mathbf{u} = \mathbf{0}$, and the Navier-Stokes equation (for the unknown pressure) can be solved analytically. Using this in (10) we get

$$\sigma K + \rho g z = \mu_0 \int_0^H M(H')dH' + \frac{\mu_0}{2}(\mathbf{M}\cdot\mathbf{n})^2 - p_0. \tag{12}$$

Thus, in the static case it remains to solve the coupled system (7), (12), which means we solve the magnetostatic potential for a given domain, calculate the magnetic forces on the free boundary, and use (12) to determine a new update for the domain. For this a parametrization of the free surface is needed. The 2d axisymmetric case in a parametric setting has been studied in [17], for the full 3d case and surfaces of graph type see [18]. From an algorithmic point of view, the big challenge in this approach is the coupling of 3d field calculations with the 2d free surface equation (12) on one cell of the developed pattern. In Fig. 10 the height of the peak over the magnetic fieldstrength for a magnetic liquid with relatively small permeability of $\mu_{\mathrm{r}} = 1.9$ is shown. Note that also the relatively small hysteresis effect, characteristic for the weak permeability, can be resolved.

The convergence of the iterative procedure has been established only numerically, it may depend from the initial shape of the unknown interface. Thus, there is some hope to calculate a single soliton by this approach over a larger domain which covers a multiple of one wave length.

Most experimentially observed phenomena of pattern formation concern the dynamic case in which the solution of the 3d Navier-Stokes equations in a time-dependent domain is needed. Now, the equations (8) and (9) are solved under the boundary conditions (10) and (11). The kinematic condition is used to find the new position of the free surface, as a consequence the nonstandard coupling of 2d/ 3d problems can be circumvented. In [21] for a single cell of an developed hexagonal pattern the dynamic into the equilibrium state is studied. It is numerically shown that the height of the peak converges if the time goes to infinity to the height of the peak of the corresponding static cases. Since both calculations are based on

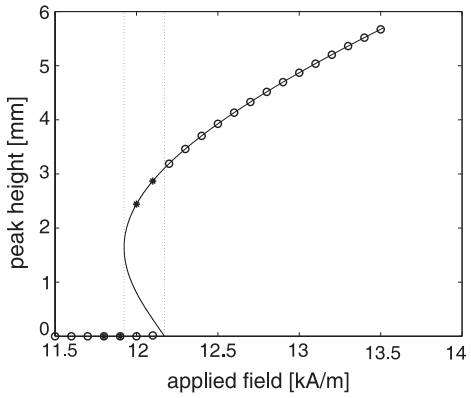

Fig. 10 Hysteresis behaviour for the magnetic fluid APG512a. The open circles (stars) mark the results for increasing (decreasing) the magnetic induction, respectively. From Ref. [18].

completely different algorithmic approaches this result is promising and gives hope for the dynamic simulation of more complicated pattern formation phenomena in the future.

3.2 Experiment

The fully developed crests of the Rosensweig pattern are much to steep to be recorded with the standard optical shadowgraphy, as used in Ref. [22] for shallow surface waves. The straightforward technique, namely the lateral observation, is only possible for zero- or one-dimensional systems [7, 23]. However, there the true profile is distorted by the meniscus at the container edges and by the field gradient induced by them. Thus we have developed a radioscopic technique which is capable to record the full surface relief with a resolution of abot 10 μm in the *center* of the vessel [24]. The experimental setup is sketched in Fig. 11(a). A Teflon® vessel with the radius of 60 mm and depth of 3 mm [12] is filled with MF up to the brim and placed on the common axis midway between two Helmholtz coils. An x-ray tube is mounted above the center of the vessel at a distance of 1606 mm. The radiation transmitted through the fluid layer and the bottom of the vessel is recorded by an x-ray sensitive photodiode array detector (16 bit). The full surface relief, as presented in Fig. 11(b) is then reconstructed from the calibrated radioscopic images. The experiments were performed with the magnetic fluid EMG 901 from Ferrotec. Its material parameters have been measured to $\mu_\mathrm{r} = 3.2$, $\rho = 1.406\,\mathrm{g\,cm^{-3}}$, and $\sigma = 25 \pm 0.7\,\mathrm{mN/m}$.

We measured the top-to-bottom amplitude A of the fluid pattern in the center of the vessel. Figure 12(a) displays the hysteretic behaviour of $A(B)$ for the adiabatic increase and decrease of B, depicted by crosses and dots, respectively. The solid and dashed lines display a fit to the roots of the amplitude equation (2), which is convincing. In comparison with the numerical results, presented in Fig. 10, we find an extended hysteretic range of about 1 mT. This is due to the higher permeability selected intentionally for the above experiments. Measurements for the fluid of Fig. 10, which allow a direct comparison are conducted in Ref. [25].

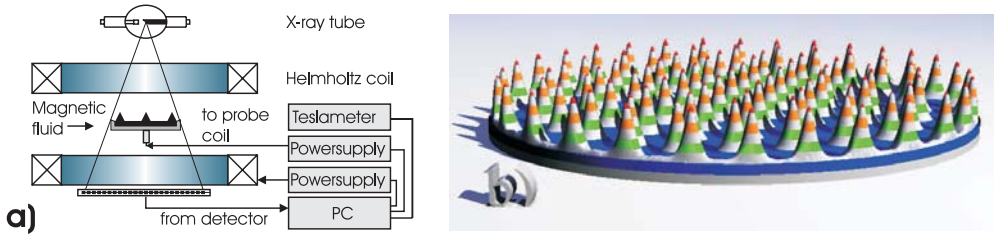

Fig. 11 Measureing the surface relief via radioscopy: (a) principle of the experimental setup (b) reconstructed surface relief. The height lines have a width of 1 mm. From Ref. [19].

Here we have realized a large hysteretic regime in order to investigate the stability of the flat surface against local perturbations within this regime. For that purpose a small air coil was placed under the center of the vessel, as depicted in Fig. 11(a). This allows to increase, locally, the magnetic induction. A local pulse of $B_+ = 0.68\mathrm{mT}$ added to the uniform field of $B = 8.91\mathrm{mT}$, produces a single stationary spike of fluid, surrounded by a circular dip, which does not disperse after B_+ has been turned off. The inset of Fig. 12(a) gives a picture of this radially-symmetric state which will be referred to as the soliton. A movie demonstrating the birth of these solitons can be accessed at Ref. [26]. The range of stability of a soliton is limited to the hysteretic regime, as marked in Fig. 12(a) by full squares and full circles.

The soliton is a stable nondecaying structure; it remained intact for days. In contrast to previously detected dissipative 2d-solitons, like oscillons [27], it is a static object without any dissipation of energy. Thus the stabilization mechanism discussed for dissipative 2d-solitons, a balance of dissipation versus nonlinearity, can not be valid here. In order to shed some light

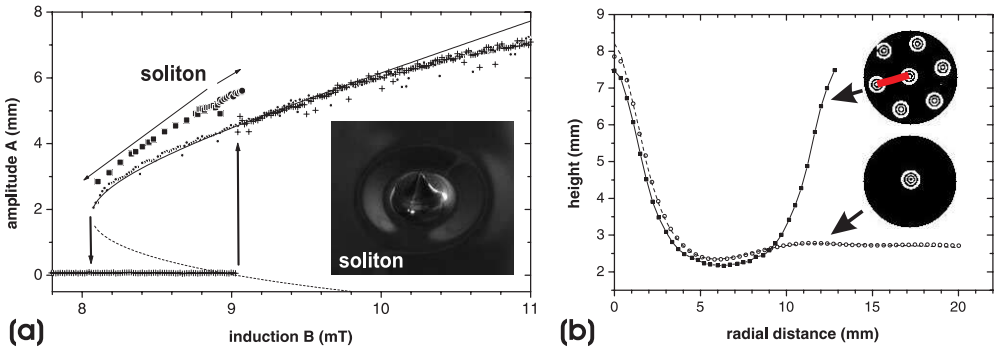

Fig. 12 (a) The amplitude of the pattern versus the magnetic induction. The crosses (dots) mark the values for increasing (decreasing) induction respectively. The solid (dashed) lines display the least square fit to the roots $A_\pm = [\gamma(1+\epsilon) \pm \sqrt{\gamma^2(1+\epsilon)^2 + 4\,\epsilon g}]/(2g)$, of the amplitude equation (2) with $\gamma = 0.281$ and $g = 0.062$. The full circles (squares) give the amplitude of the localized spike initiated at $B = 8.91\mathrm{mT}$ for increasing (decreasing) induction respectively. (b) Hight profiles for one periode of the hexagonal pattern (filled squares), and for two different solitons (marked by open symbols and a dashed line). From Ref. [19].

at its mechanism of stabilization we compare in Fig. 12(b) the azimuthally averaged hight profile of solitons with the one of regular Rosensweig peaks. In agreement with Fig. 12(a) the soliton is about 1 mm taller than the spike of the lattice. This may be attributed to the fact, that the spikes emerge simultaneously, and thus have to share the liquid available. Most importantly, the width of the soliton is equal to the period of the lattice. Therefore there is a preferred wavelength in the system, defined by the lattice, and the soliton locks to this wavelength. Utilizing a conservative analogue of the Swift-Hohenberg equation we have been able to show in Ref. [19] that this width locking is the central part of the solitons stabilization mechanism.

To conclude, we have demonstrated, that a quantitative comparsion of results generated by clean experiments, suitable numerical simulations and the analytical theory, opens a way for a deeper understanding of the physical phenomena in surface instabilities.

Acknowledgements The authors would like to thank Igor Barashenkov, Andreas Engel, René Friedrichs, Edgar Knobloch, Gunar Matthies, Ingo Rehberg, Wim van Saarloos, and Mark Shliomis for interesting and clarifying discussions and Bert Reimann for performing the experiments in section 2. The work was supported by the *Deutsche Forschungsgemeinschaft* under grants FOR 301, La 1182/2, Ri 1054/1, and To 143/4.

References

[1] A. Gailitis, J. Fluid Mech. **82**, 401 (1977).
[2] R. Friedrichs and A. Engel, Phys. Rev. E **64**, 021406 (2001).
[3] M. D. Cowley and R. E. Rosensweig, J. Fluid Mech. **30**, 671 (1967).
[4] R. E. Rosensweig, *Ferrohydrodynamics* (Cambridge University Press, Cambridge, 1985).
[5] R. Richter, B. Reimann, A. Lange, P. Rupp, and A. Rothert, Advances in Solid State Physics **43**, 789 (2003).
[6] R. Friedrichs, Ph.D. thesis, Universität Magdeburg, 2003.
[7] J.-C. Bacri and D. Salin, J. Phys. (France) **45**, L559 (1984).
[8] A. Boudouvis, J. Puchalla, L. Scriven, and R. Rosensweig, J. Magn. Magn. Mater. **65**, 307 (1987).
[9] A. Lange, B. Reimann, and R. Richter, Magnetohydrodynamics **37**, 261 (2001).
[10] D. Salin, Europhys. Lett. **21**, 667 (1993).
[11] A. Lange, B. Reimann, and R. Richter, Phys. Rev. E **61**, 5528 (2000).
[12] B. Reimann, R. Richter, I. Rehberg, and A. Lange, Phys. Rev. E **68**, 036220 (2003).
[13] J. Weilepp and H. R. Brand, J. Phys. II France **6**, 419 (1996).
[14] B. Abou, G. Néron de Surgy, and J. E. Wesfreid, J. Phys. II France **7**, 1159 (1997).
[15] H. W. Müller, Phys. Rev. E **55**, 6199 (1998).
[16] T. Mahr, Ph.D. thesis, Otto-von-Guericke Universität Magdeburg, 1998.
[17] V. G. Bashtovoi, O. A. Lavrova, V. K. Polevikov, and L. Tobiska, J. Magn. Magn. Mater. **252**, 299 (2002).
[18] O. Lavrova, G. Matthies, T. Mitkova, V. Polevikov, and L. Tobiska, Lect. Notes Comput. Sci. Eng. **35**, 160 (2003).
[19] R. Richter and I. Barashenkov, Phys. Rev. Lett. **94**, 184503 (2005).
[20] O. Lavrova, G. Matthies, V. Polevikov, and L. Tobiska, PAMM Proc. Appl. Math. Mech. **4**, 704 (2004).
[21] G. Matthies and L. Tobiska, J. Magn. Magn. Mater. **289**, 346 (2005).
[22] J. Browaeys, J.-C. Bacri, C. Flament, S. Neveu, and R. Perzynski, Eur. Phys. J. B **9**, 335 (1999).
[23] T. Mahr and I. Rehberg, Phys. Rev. Let. **81**, 89 (1998).
[24] R. Richter and J. Bläsing, Rev. Sci. Instrum. **72**, 1729 (2001).
[25] C. Gollwitzer, G. Matthies, R. Richter, I. Rehberg, and L. Tobiska, J. Fluid Mech. **571**, 455 (2007).
[26] D. Castellvecchi, Physical Review Focus, http://focus.aps.org/story/v15/st18 , (2005).
[27] P. B. Umbanhowar, F. Melo, and H. L. Swinney, Nature (London) **382**, 793 (1996).